The Astrophysical Journal Letters, 1006:L8 (13pp), 2026 July 20 https://doi.org/10.3847/2041-8213/ae80bc

First Detection of Faraday Rotation in a Gamma-Ray Burst Afterglow: Low Polarization and High Rotation Measure in GRB 260310A Reveal the Jet's Magnetic Structure and Environment

Collin T. Christy[1], Tanmoy Laskar[2], Kate D. Alexander[1], Noah Franz[1], Jonathan Granot[3,4,5], Ryan Chornock[6,7], Raffaella Margutti[6,7,8], Ramandeep Gill[4,9], Jeniveve Pearson[1], Edo Berger[10], Wen-fai Fong[11,12], Coleman Rohde[2], and Patricia Schady[13]

[1] Steward Observatory, University of Arizona, 933 North Cherry Avenue, Tucson, AZ 85721-0065, USA; collinchristy@arizona.edu
[2] Department of Physics & Astronomy, University of Utah, Salt Lake City, UT 84112, USA
[3] Department of Natural Sciences, The Open University of Israel, P.O Box 808, Ra'anana 4353701, Israel
[4] Astrophysics Research Center of the Open University (ARCO), The Open University of Israel, P.O Box 808, Ra'anana 43537, Israel
[5] Department of Physics, The George Washington University, 725 21st Street NW., Washington, DC 20052, USA
[6] Department of Astronomy, University of California, Berkeley, CA 94720-3411, USA
[7] Berkeley Center for Multi-messenger Research on Astrophysical Transients and Outreach (Multi-RAPTOR), University of California, Berkeley, CA 94720-3411, USA
[8] Department of Physics, University of California, 366 Physics North MC 7300, Berkeley, CA 94720, USA
[9] Instituto de Radioastronomía y Astrofísica, Universidad Nacional Autónoma de México, Morelia, Michoacán, C.P. 58089, México
[10] Center for Astrophysics | Harvard & Smithsonian, Cambridge, MA 02138, USA
[11] Center for Interdisciplinary Exploration and Research in Astrophysics and Department of Physics and Astronomy, Northwestern University, 1800 Sherman Ave., 8th Floor, Evanston, IL 60201, USA
[12] Department of Physics and Astronomy, Northwestern University, Evanston, IL 60208, USA
[13] Department of Physics, University of Bath, Claverton Down, Bath BA2 7AY, UK
Received 2026 April 30; revised 2026 June 16; accepted 2026 June 18; published 2026 July 14

Abstract

We report the detection of linear polarization in the radio afterglow of GRB 260310A, representing the first centimeter-wavelength polarization detection of a gamma-ray burst (GRB) afterglow and the first measurement of Faraday rotation in a GRB environment. We detect linearly polarized emission across 11–25 GHz, with a polarization fraction decreasing monotonically from $(3.18 \pm 0.18)\%$ at 25 GHz to $(0.69 \pm 0.22)\%$ at 11 GHz. We model the multiwavelength data as emission from a refreshed forward shock (FS) that dominates in the optical and X-rays and a reverse shock (RS) in a structured, relativistic jet that dominates at radio wavelengths. The observed depolarization toward the lower radio frequencies is consistent with suppression by RS synchrotron self-absorption, while the low observed polarization at high frequencies relative to the theoretical maximum suggests a patchy magnetic field in the jet with a coherence scale, $\theta_B \approx 10^{-2}$ rad. We identify a frequency-dependent rotation of the polarization angle consistent with Faraday rotation, with a rotation measure (RM) of $\mathrm{RM} = -(8300 \pm 90)\ \mathrm{rad\ m^{-2}}$ at the GRB redshift. The magnitude of the RM is consistent with propagation through a dense, magnetized environment, such as a progenitor H II region. These findings demonstrate that GRB afterglows exhibit measurable linear polarization at centimeter wavelengths, and that their polarimetric properties probe both intrinsic jet magnetization and the surrounding medium. Future multifrequency polarimetric monitoring over timescales of days to weeks will enable detailed studies of the evolution of magnetic field structure and provide new constraints on the role of magnetic fields in GRB afterglows.

Unified Astronomy Thesaurus concepts: Gamma-ray bursts (629); Relativistic jets (1390); Radio astronomy (1338)

1. Introduction

Magnetized relativistic jets are ubiquitous in extreme accretion environments across a range of mass scales, from stellar-mass compact objects to supermassive black holes (SMBHs) in active galactic nuclei (AGN). However, in spite of their prevalence, the fundamental physics governing their formation, collimation, and magnetization remain poorly understood (P. Mészáros 2006; P. Kumar & B. Zhang 2015). Long-duration gamma-ray bursts (GRBs) resulting from the core collapse of massive stars offer a unique laboratory for addressing these key questions, as their extreme luminosity and large bulk Lorentz factors ($\Gamma \sim 10^2$–10^3) make them ideal probes for jet physics observable on human timescales (P. Meszaros & M. J. Rees 1993; M. J. Rees & P. Meszaros 1994; D. A. Frail et al. 1997; S. E. Woosley & J. S. Bloom 2006).

Synchrotron polarization from GRB afterglows offers a window into the magnetic field geometry of jetted systems. The afterglow itself is generated by the interaction of the jet with the immediate circumburst environment, producing two shocks: a long-lived relativistic forward shock (FS) in the ambient medium powering the broadband afterglow, and a short-lived reverse shock (RS) propagating back through the decelerating ejecta (R. Sari & T. Piran 1995; S. Kobayashi & B. Zhang 2003a). Both of these shocks accelerate electrons and generate synchrotron emission, whose polarization directly encodes the magnetic field geometry. Ordered fields are expected to yield high RS linear polarization ($\Pi_{RS} \gtrsim 70\%$), while tangled fields produce low polarization ($\Pi_{\rm RS} \lesssim 10\%$) that depends on the anisotropy of the magnetic fields (A. Gruzinov & E. Waxman 1999; J. Granot 2003; J. Granot & A. Königl 2003; J. Granot & G. B. Taylor 2005). FS linear polarization, meanwhile, is sensitive to jet angular structure and viewing geometry through its behavior around the jet-break time, providing complementary constraints on whether the jet has, e.g., a top-hat, power-law, or Gaussian energy profile (J. D. Salmonson 2003; E. M. Rossi et al. 2004; G. Birenbaum et al. 2026).

Multifrequency polarization observations can provide additional information via the detection of Faraday rotation, which is observed regularly in AGN (e.g., T. Hovatta et al. 2012; D. C. Gabuzda et al. 2015; E. V. Kravchenko et al. 2017), fast radio bursts (e.g., D. Michilli et al. 2018; Y.-P. Yang et al. 2023), and Galactic sources (e.g., R. J. Rand & S. R. Kulkarni 1989; H. Ohno & S. Shibata 1993; J. L. Han et al. 2004). Faraday rotation, which manifests as a rotation of the polarization position angle with frequency, directly constrains the line-of-sight (LOS) magnetic field strength and electron density of the intervening medium (B. J. Burn 1966). This provides a direct probe of the magnetic field conditions intrinsic to the afterglow-emitting region or the intervening circumburst and host galaxy environments and may constrain GRB progenitor models (J. Granot & G. B. Taylor 2005; R. Gill et al. 2021).

Optical and near-infrared polarimetric observations of GRB afterglows have yielded successful detections in a handful of events (e.g., S. Covino et al. 1999; E. Rol et al. 2000; G. Björnsson et al. 2002; A. J. Barth et al. 2003; D. Bersier et al. 2003; D. Lazzati et al. 2003; E. Maiorano et al. 2006; C. G. Mundell et al. 2013; K. Wiersema et al. 2014; S. Covino & D. Gotz 2016; I. A. Steele et al. 2017; M. Arimoto et al. 2024). In most cases, the earliest ($<10^3$ s) and most highly polarized ($10\% \lesssim \Pi_L \lesssim 30\%$) detections are likely dominated by RS emission (R. Gill et al. 2021). As the optical emission becomes dominated by FS emission, the intrinsic polarized RS emission can be diluted by the weakly polarized FS component, as proposed for GRB 120308A (C. G. Mundell et al. 2013).

As RS emission persists longest at low frequencies, it is natural to search for RS polarization signatures in the radio and millimeter bands. Historically, radio polarization searches in GRBs have mostly yielded upper limits (e.g., J. Granot & G. B. Taylor 2005; A. van der Horst et al. 2014; Y. Urata et al. 2023), in part due to the limited sensitivity of millimeter-/centimeter-band facilities and the large cosmological distances of most events. This changed with the first Atacama Large Millimeter/submillimeter Array (ALMA) detection of linearly polarized emission (≈1%) from the nearby (z = 0.4245) GRB 190114C (T. Laskar et al. 2019a), which demonstrated that GRB RSs are polarized at millimeter wavelengths. These observations constrained the magnetic field coherence scale in the ejecta, inferred in this case to be $\theta_B \approx 10^{-3}$ rad, which is at least ∼10 times smaller than suggested by the large 28% ± 4% polarization of the early 240–323 s optical afterglow of GRB 120308A (C. G. Mundell et al. 2013), showing significant diversity in the GRB population. However, GRB 190114C's afterglow faded quickly, enabling only one constraining single-band polarimetry observation within hours of the GRB discovery.

Here, we present radio polarimetry observations of the recent GRB 260310A, which, due to its proximity, has one of the brightest radio afterglows seen in decades. We report the first multifrequency detection of linear polarization in a GRB afterglow, extending radio polarimetry into the centimeter band and opening a new observational window into GRB jet magnetization and structure. Additionally, the position angle exhibits Faraday rotation with frequency, marking the first detection of this effect in a GRB and revealing information about the GRB's environment.

We structure our Letter as follows. In Section 2, we summarize the basic properties of GRB 260310A, compile relevant public multiwavelength observations from the community, and present our radio observations and data reduction procedure. We model the multiwavelength photometry and the radio polarization in Section 3 and interpret these findings jointly in Section 4. We conclude in Section 5. Unless otherwise specified, frequencies and times are in the observer frame. For our analysis, we assume a cosmology of $\Omega_M = 0.31$, $\Omega_\Lambda = 0.69$, and h = 0.68, and a luminosity distance at z = 0.153 of 745 Mpc.

2. Observations

2.1. Basic Properties and Community Data: General Coordinates Network

GRB 260310A triggered the Fermi Gamma-ray Burst Monitor (GBM) at 04:57:10 UT on 2026 March 10 (Fermi GBM team 2026); all times reported in our subsequent analysis are measured relative to this time. The prompt gamma-ray emission consists of a single primary pulse with $T_{90} \sim 60$ s (50–300 keV; R. Hamburg & C. Meegan 2026) and was also detected by AstroSAT CZTI, consistent with a standard long GRB (P. Minaev et al. 2026; S. K. H. H. Salunke et al. 2026). The afterglow was subsequently detected in the optical (K. Hinds et al. 2026; R. Konno et al. 2026; D. O'Neill et al. 2026), X-rays (R. Jayaraman et al. 2026a), and radio (S. Giarratana et al. 2026; A. Y. Q. Ho et al. 2026; D. A. Perley et al. 2026; L. Rhodes et al. 2026; G. Schroeder et al. 2026). Shortly after, a spectroscopic redshift of z = 0.153 was reported and confirmed by multiple groups (A. de Ugarte Postigo et al. 2026a; K.-R. Hinds et al. 2026; B. Hsu et al. 2026). The transient is located in the outskirts of its host galaxy with a separation from the nucleus of $\approx 5\farcs9$ (∼20 kpc; see Figure 1). At this redshift, the peak energy, $E_{\rm peak} = (172 \pm 5)$ keV, cutoff power-law index $=5.8 \pm 0.4$, and fluence $(5.8 \pm 0.4) \times 10^{-6}$ erg cm^{-2} (10–1000 keV, observer frame; R. Hamburg & C. Meegan 2026) correspond to an isotropic-equivalent γ-ray energy of $E_{\gamma,\rm iso} = (3.4 \pm 0.2) \times 10^{50}$ erg (1–10^4 keV, rest frame). These energetics place GRB 260310A in the compact object merger region of the $E_{p,i} - E_{\rm iso}$ relation (L. Amati 2006; J.-L. Atteia et al. 2026), which is unusual but not unprecedented for long-duration GRBs (e.g., GRB 211211A; J. C. Rastinejad et al. 2022; E. Troja et al. 2022). Continued spectroscopic follow-up of this event revealed an emerging Type Ic broad-line (Ic-BL) supernova component, SN 2026fgk (A. de Ugarte Postigo et al. 2026b; M. Freeberg et al. 2026; M. Guelfand et al. 2026; B. O'Connor et al. 2026), securing a connection to the collapse of a massive star.

To provide a broader multiwavelength context for our polarization observations (Section 2.2), we utilize a subset of the public radio, optical, and X-ray photometry[14] reported by

[14] The X-ray light curve exhibits a rebrightening at $\gtrsim 30$ days posttrigger (R. Jayaraman et al. 2026b; G. Waratkar et al. 2026; Y. Yang et al. 2026), which cannot be explained with a standard afterglow model. We defer a discussion of these data to future work.

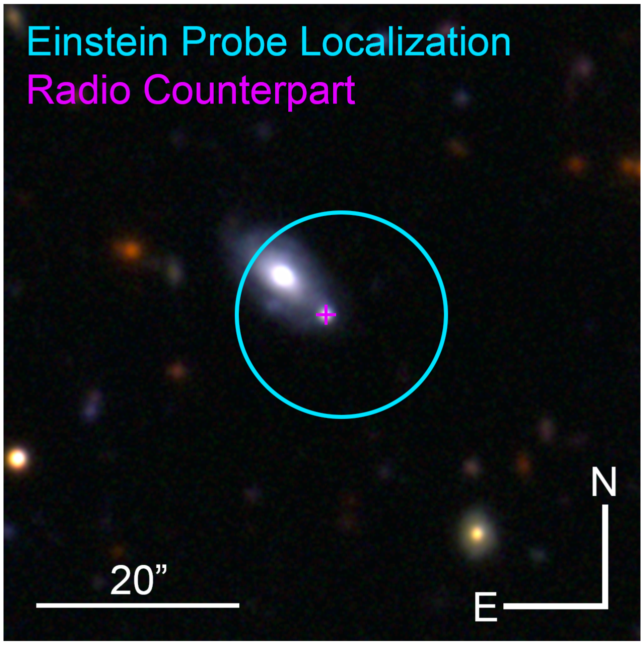

Figure 1. MMT Binospec *gri* color image of GRB 260310A taken on 2026 April 18, ∼39.2 days posttrigger. The coordinates of our Very Large Array (VLA) detection are shown as a purple cross and are consistent with the optical position. The statistical error on the radio position is smaller than the systematic astrometric accuracy of ∼10 mas typically achievable by the VLA in A configuration. For comparison, the Einstein Probe 90% localization region of the GRB is shown as a blue circle (R. Jayaraman et al. 2026a).

the community in General Coordinates Network (GCN) circulars (R. L. Becerra et al. 2026; R. Brivio et al. 2026; A. Brosio et al. 2026a, 2026b; S. Giarratana et al. 2026; A. Ho et al. 2026; A. Y. Q. Ho et al. 2026; L. Izzo 2026; R. Jayaraman et al. 2026a, 2026c; E. Kammoun et al. 2026; R. Konno et al. 2026; C.-H. Lai et al. 2026; J.-J. Li et al. 2026; A. Martin-Carrillo et al. 2026a, 2026b; E. M. Méndez et al. 2026; A. Moskvitin et al. 2026; N. Pankov et al. 2026; N. Passaleva et al. 2026a, 2026b; D. A. Perley et al. 2026a, 2026b; M. Pursiainen et al. 2026; L. Rhodes et al. 2026; G. Schroeder et al. 2026; M. Serrau et al. 2026; R. Stein et al. 2026; A. Volnova et al. 2026; A. M. Watson et al. 2026). We also use optical polarimetric observations conducted by M. Pursiainen et al. (2026) at 2.89 days posttrigger, which resulted in a linear polarization upper limit of $\Pi_L < 1.5\%$ (3σ, not corrected for Galactic interstellar polarization). We exclude optical photometry at $t > 15.2$ days, as these observations deviate from the power-law decline, indicating the emergence of an underlying supernova (M. Guelfand et al. 2026).

2.2. Very Large Array Polarization Observations

On 2026 March 29 (19.2 days), we observed GRB 260310A ($\alpha = 14^{\rm h}37^{\rm m}16\overset{\rm s}{.}14$, $\delta = +71°50'30''.30$; J2000) with the Karl G. Jansky Very Large Array (VLA) under program VLA/26A-032 (PI: T. Laskar). We performed a three-hour continuum observation using 3-bit samplers at bands *X* (10 GHz), *Ku* (15 GHz), and *K* (22 GHz). We observed 3C286 as the bandpass, flux, and polarization angle calibrator, J1407+2827 as a low-polarization leakage calibrator, and J1357+7643 as the complex gain calibrator.

We processed the data with the Common Astronomy Software Application (CASA 6.7.0.31; CASA Team et al. 2022). We first calibrated the parallel-hand (RR/LL, where R and L are the right and left circular polarizations) cross-correlation visibilities using the NRAO pipeline (v6.4.1.12). We then reapplied the pipeline calibration solutions with the parallactic angle corrections disabled. For the polarization calibration, we first corrected for the instrumental delay between the cross hands (RL/LR) using the bandpass calibrator separately for each baseband. We then solved for the instrumental frequency-dependent leakage terms (D-terms) using the low-polarization source J1407+2827. Finally, we solved for the frequency-dependent R-L phase per antenna using a polarization model of 3C286 constructed from polynomial fits to the tabulated flux densities, polarization fractions, and polarization angles provided by NRAO.[15]

For the target field, we performed phase-only self-calibration on Stokes *I*, with the derived phase solutions subsequently applied to all Stokes parameters. The effect on the measured flux density was modest ($\lesssim$5% across all bands), with the largest corrections occurring at the highest frequencies. We imaged the data using the CASA task `tclean` and obtained flux densities and their uncertainties by using the CASA task `imfit` to fit an elliptical Gaussian fixed to the size of the synthesized beam. For estimating Stokes *Q* and *U* flux densities, we fixed the position of the elliptical Gaussian to the source location measured in the Stokes *I* image. We discuss additional calibration checks performed on the data in Appendix A. We present the *I*, *Q*, *U*, and $P_L = \sqrt{Q^2 + U^2}$ Stokes images in Figure 2.

We detect linearly polarized emission from GRB 260310A from 11 to 25 GHz (Table 1). The polarization fraction drops slowly from (3.18 ± 0.18)% at 25 GHz to (1.99 ± 0.13)% at 15 GHz, and then plummets to undetectable values (<0.6%, 3σ) at 9 GHz (Figure 3, left panels). Our lowest significant polarization detection of (0.69 ± 0.22)% is at 11 GHz, which coincides with the peak of the Stokes *I* spectrum.

While our observations at 19.2 days do not fully sample the low-frequency segment, VLA observations at 17.2 days reveal a steep low-frequency spectrum[16] with $\beta = 1.37 \pm 0.02$ (D. A. Perley et al. 2026a). This steeply rising spectrum indicates that the emission likely experiences strong synchrotron self-absorption (SSA). Assuming the spectral peak is the SSA break ($\nu_{\rm sa}$), we fit the observed depolarization as a function of frequency (see Appendix B, Equation (B11)) with the intrinsic linear polarization on the optically thin segment (Π_0) as a free parameter. We find that this model reproduces the $\Pi_L(\nu)$ spectrum well for $\Pi_0 = (3.2 \pm 0.2)\%$ and the electron energy index, $p = 2.7^{+0.8}_{-0.5}$, and predicts $\nu_{\rm sa} = (13.3 \pm 0.5)$ GHz, roughly consistent with the peak of the Stokes *I* spectrum and providing further evidence that the observed depolarization is attributable to SSA.

We find no evidence of temporal evolution in the measured polarized intensities during our observations. However, given the relatively short time on source (∼10, 25, and 45 minutes in the *X*, *Ku*, and *K* bands, respectively) at ∼19 days postburst, these observations span a very small fraction of the afterglow age ($\Delta t/t \lesssim 0.001$). We therefore cannot meaningfully constrain whether the polarization fraction or position angle evolve with time.

[15] https://science.nrao.edu/facilities/vla/docs/manuals/obsguide/modes/flux-density-scale-polarization-leakage-polarization-angle-tables
[16] We use the convention $F_\nu \propto t^\alpha \nu^\beta$ throughout.

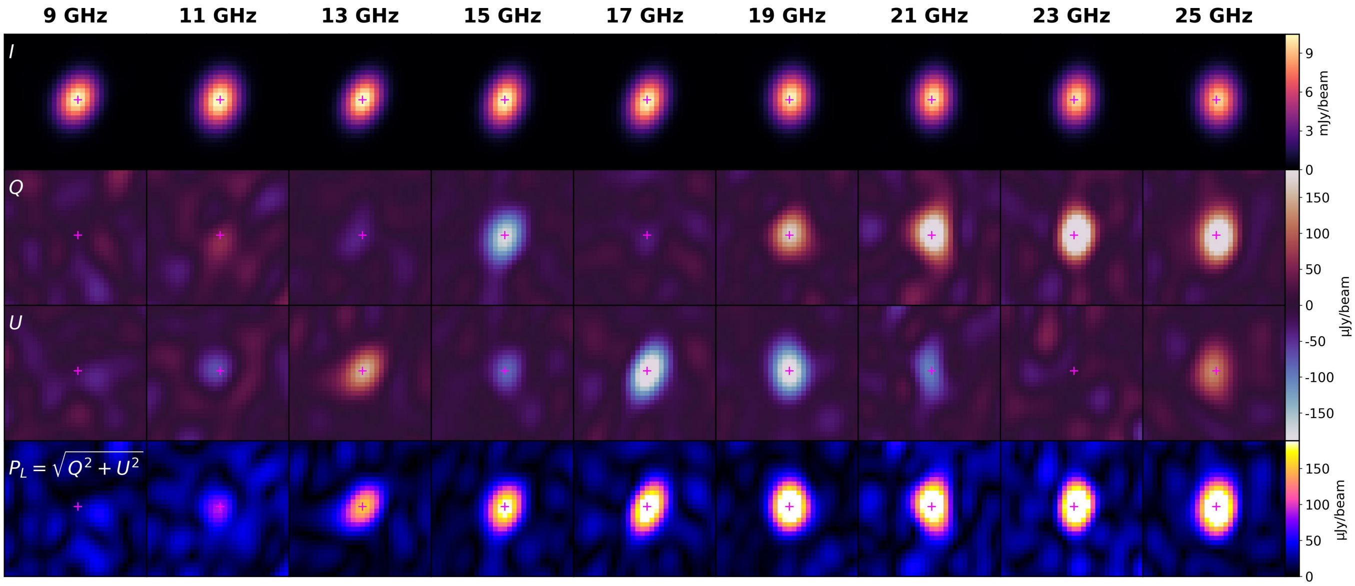

Figure 2. Stokes IQU and linear polarization intensity $P_L = \sqrt{Q^2 + U^2}$ of GRB 260310A at 19.2 days. The images reveal a strong polarized point source that fades at lower frequencies. Additionally, the QU images reveal a frequency-dependent rotation in the polarization angle.

2.3. Faraday Rotation

In Figure 3, we show the variation of the Stokes Q and U flux densities as a function of frequency. The polarized intensity and position angle, $\chi = \frac{1}{2}\arctan(U/Q)$, exhibit a spiral pattern characteristic of Faraday rotation combined with frequency-dependent depolarization. The rate at which the polarization position angle traverses this spiral yields the rotation measure (RM):

$$\chi = \chi_0 + \mathrm{RM}\,\lambda^2. \tag{1}$$

After removing 2π wraps, we find that a plot of χ versus λ^2 (Figure 3, lower-right panel) is well fit ($R^2 = 0.999$) with a straight line, yielding[17] $\mathrm{RM} = -(6250 \pm 70)\,\mathrm{rad\,m^{-2}}$.

To determine whether this observed RM is intrinsic to the source, we estimate the expected Faraday rotation from the Milky Way (MW) and the intergalactic medium (IGM). GRB 260310A is located at Galactic coordinates, $l = 111\overset{\circ}{.}99$, $b = 42\overset{\circ}{.}97$, and, at these intermediate Galactic latitudes, all-sky maps of Galactic Faraday depths suggest that the MW contribution to the observed RM is very modest, with $\mathrm{RM_{MW,GRB}} = -(1.12 \pm 8.15)\,\mathrm{rad\,m^{-2}}$ (N. Oppermann et al. 2012).

Our data reduction process used the known $\chi(\nu)$ for 3C286 to calibrate χ for the target. This process corrects for the $\mathrm{RM_{MW}}$ contribution along the 3C286 LOS, $\mathrm{RM_{MW,3C286}} = (2.52 \pm 2.77)\,\mathrm{rad\,m^{-2}}$ (N. Oppermann et al. 2012). Since the 3C286 LOS ($l = 56\overset{\circ}{.}52$, $b = 80\overset{\circ}{.}67$) is separated from that of GRB 260310A by $\sim 42°$, the two probe independent regions of the Galactic foreground. Even accounting for this difference, however, we find that the net systematic $\mathrm{RM_{MW}}$ offset for the GRB LOS is negligible, $\mathrm{RM_{MW,GRB}} - \mathrm{RM_{MW,3C286}} \approx -(3.6 \pm 8.6)\,\mathrm{rad\,m^{-2}}$ ($\lesssim 0.1\%$ of the observed RM). Similarly, the Faraday rotation contribution from the IGM is expected to be small, with current estimates yielding $|\mathrm{RM_{IGM}}| \lesssim 10\,\mathrm{rad\,m^{-2}}$ (e.g., J. P. Vallee 1975; P. P. Kronberg & M. Simard-Normandin 1976; T. Vernstrom et al. 2019; S. Mtchedlidze et al. 2024). The combined Galactic foreground and IGM contribution along the GRB LOS is therefore of the order of $\pm 10\,\mathrm{rad\,m^{-2}}$.

We further verified this by examining the RM of the phase calibrator J1357+7643 (Figure 5 in Appendix A), which exhibits a modest $|\mathrm{RM}| \approx 60\,\mathrm{rad\,m^{-2}}$. Given the small angular separation between the phase calibrator and GRB 260310A ($\sim 5°$), both sight lines probe a similar region of the Galactic foreground and IGM. Comparing to the total MW+IGM contribution computed above would imply that the bulk of the phase calibrator's RM is intrinsic to the source itself, but even if we assume the full $\mathrm{RM} \approx -60\,\mathrm{rad\,m^{-2}}$ is due to the MW and IGM along the LOS to the phase calibrator, this is still 2 orders of magnitude below our observed GRB $|\mathrm{RM}| \approx 6.3 \times 10^3\,\mathrm{rad\,m^{-2}}$. We therefore conclude that the observed RM of the GRB polarization originates from a Faraday screen local to GRB 260310A or its host galaxy. This implies an intrinsic $\mathrm{RM_{int}} = (1 + z)^2 RM \approx -8.3 \times 10^3\,\mathrm{rad\,m^{-2}}$ at the source redshift.

3. Afterglow Modeling

For a physical interpretation of our polarimetric measurements, we now discuss the multiwavelength afterglow emission in the standard formalism, in which the RS and FS produce synchrotron radiation via relativistic electrons accelerated to a power-law distribution in energy (with index, p). We assume that a fraction ϵ_e of the postshock energy is imparted to relativistic electrons and a fraction ϵ_B to magnetic fields. The isotropic-equivalent kinetic energy of the jet (with a collimation angle, $\theta_{\rm jet}$) is $E_{\rm K,iso}$. We assume that the circumstellar medium (CSM) at radius R has a power-law density profile, $\rho = AR^{-k}$, which can be cast in terms of the parameter A_* as $A = 5 \times 10^{11} A_*\,\mathrm{g\,cm^{-1}}$ for a wind-like CSM ($k = 2$). The spectrum of each emission component (RS and FS) is characterized by (e.g., R. Sari 1997; R. Sari &

[17] For this RM, the fractional depolarization due to bandwidth averaging, $\frac{1}{\Delta\nu}|\int_{\nu_0}^{\nu_0+\Delta\nu} e^{2i\chi(\nu)} d\nu|$, is small ($\lesssim 10\%$) over a 2 GHz bandwidth at $\gtrsim 13$ GHz. This can rise to $\approx 25\%$ at ≈ 11 GHz; however, we find that splitting the bandwidth into smaller chunks and reimaging does not significantly change the shape of $\chi(\nu)$, indicating that the depolarization observed at low frequencies is intrinsic and not due to bandwidth effects.

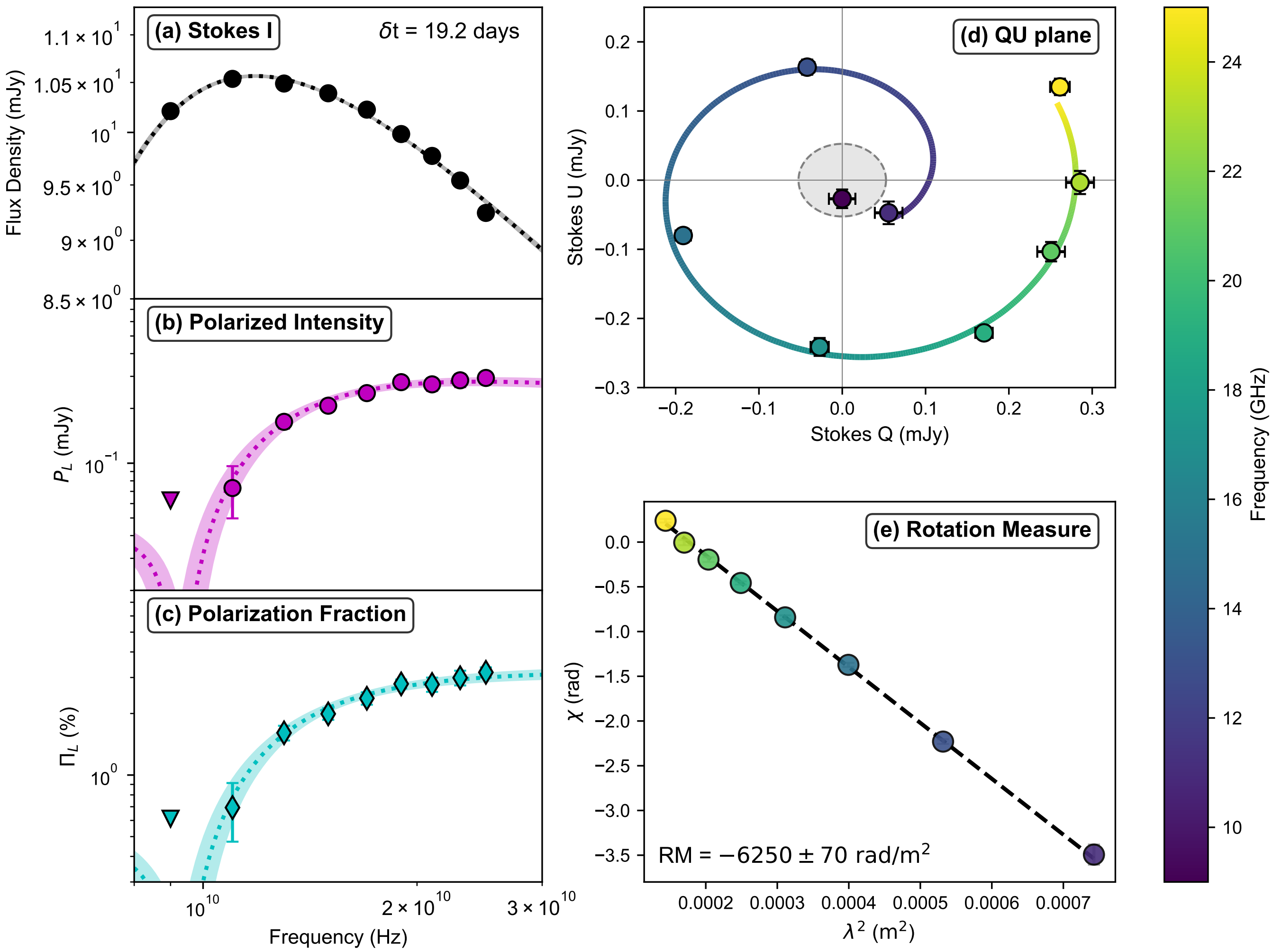

Figure 3. (a) The measured flux density of Stokes I, (b) the linear polarization flux density, and (c) the linear polarization fraction Π_L as a function of frequency. We show the best-fitting model (Equation (B11); dotted lines, shaded regions are 1σ posteriors), which show a constant linear polarization intensity and fraction that decays exponentially to lower frequencies. (d) We show the Stokes U versus Q colorized by observed frequency. The data exhibit a spiral structure indicative of Faraday rotation. The solid line shows the depolarization frequency response derived from Equation (B11), and the shaded region indicates the average 3σ detection threshold for P_L. (e) The polarization angle $\chi = (1/2)\arctan(U/Q)$ as a function of λ^2. The data reveal a steep slope corresponding to a rotation measure (RM) of $|\mathrm{RM}| \approx 6.3 \times 10^3$ rad m^{-2}, indicative of a highly ordered magnetic field structure along the LOS.

Table 1
Measured Stokes Flux Densities

$\nu_{\rm obs}$ (GHz)	I (mJy)	Q (μJy)	U (μJy)	P_L (μJy)	Π_L (%)	χ (rad)
9	10.21 ± 0.02	0 ± 16	−27 ± 13	27 ± 21	< 0.6	⋯
11	10.54 ± 0.02	56 ± 17	−47 ± 16	73 ± 23	0.69 ± 0.22	−3.49 ± 0.11
13	10.49 ± 0.01	−42 ± 9	163 ± 11	169 ± 14	1.61 ± 0.13	−2.23 ± 0.03
15	10.39 ± 0.01	−191 ± 9	−80 ± 10	207 ± 13	1.99 ± 0.13	−1.37 ± 0.02
17	10.23 ± 0.01	−27 ± 11	−241 ± 13	243 ± 17	2.37 ± 0.17	−0.84 ± 0.02
19	9.98 ± 0.01	170 ± 10	−221 ± 9	279 ± 14	2.79 ± 0.14	−0.46 ± 0.02
21	9.77 ± 0.03	251 ± 17	−103 ± 14	271 ± 22	2.77 ± 0.22	−0.20 ± 0.03
23	9.54 ± 0.03	285 ± 17	−3 ± 17	285 ± 24	2.99 ± 0.25	−0.01 ± 0.03
25	9.24 ± 0.02	261 ± 12	135 ± 12	294 ± 17	3.18 ± 0.18	0.24 ± 0.02

Note. Uncertainties are 1σ and statistical only, and upper limits are 3σ. We show the total intensity I, Stokes parameters Q and U, linear polarized flux density $P_L = \sqrt{Q^2 + U^2}$, fractional linear polarization $\Pi_L = P_L/I$, and polarization angle $\chi = \frac{1}{2}\arctan(U/Q)$.

T. Piran 1999; J. Granot & R. Sari 2002) a self-absorption break ($\nu_{\rm sa}$), a characteristic frequency (ν_m), and a synchrotron cooling break (ν_c).

3.1. Afterglow Evolution: Optical and X-Rays

We find that the optical and X-ray light curves are challenging to interpret in this framework. The consolidated

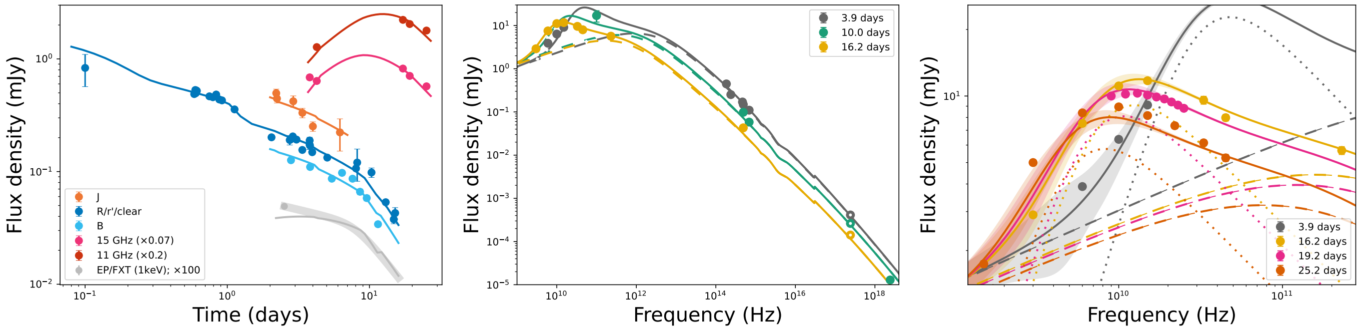

Figure 4. Multiwavelength radio to X-ray light curves at ≈0.1–25 days (left), and spectral energy distributions (center; extrapolated Einstein Probe Follow-up X-ray Telescope points are shown as open symbols) with a zoom in to the radio (right) for GRB 260310A with an FS model in a wind environment including two episodes of energy injection (dominating in the optical and X-rays; dashed) and an RS in a structured jet (dominating at radio wavelengths; dotted, right panel). The shaded regions indicate the 1σ scatter expected from interstellar scintillation along this sight line.

R/r'-band optical light curve (Figure 4) from 3.0 to 15.2 days can be fit with a broken power law, breaking from $\alpha_r = -0.65 \pm 0.1$ to -2.5 ± 1.0 at 10.8 ± 1.4 days. The shallowest possible decay of $\alpha = (3–3p)/4$, afforded by a uniform-density[18] environment ($k = 0$) in the regime $\nu_m < \nu_{\rm opt} < \nu_c$, nevertheless still implies an unusually low value of $p = 1.8 \pm 0.1$ and predicts an optical spectral index of $\beta = (1 - p)/2 \sim -0.4$, which is ruled out by steeper $\beta_{\rm opt} = -0.9 \pm 0.1$ inferred from a power-law fit to the B-band to H-band photometry at ≈3.9 days.

The X-ray light curve evolves from $\alpha_{\rm X,1} \approx -0.3$ to $\alpha_{\rm X,2} \approx -1.6$ at (8 ± 2) days (R. Jayaraman et al. 2026c). The optical and X-ray decay rates from 3 to 8 days appear consistent within the uncertainties. Extrapolating the B- to J-band optical spectral energy distribution (SED) at ≈3.6 days (derived from L. Izzo 2026; C.-H. Lai et al. 2026; J.-J. Li et al. 2026; A. Martin-Carrillo et al. 2026a; A. Moskvitin et al. 2026) to the X-rays gives a flux consistent with the X-ray light curve at this time. Furthermore, the X-ray spectral index,[19] $\beta_{\rm X} = -0.76 \pm 0.22$ (E. Kammoun et al. 2026), is consistent with $\beta_{\rm opt}$. Together, these three observations indicate that the optical and X-rays are on the same synchrotron segment.

The quasi-monochromatic optical/X-ray break at ≈10 days and the steep postbreak decay are consistent with a jet break ($\alpha \approx -p$), suggesting $p \approx 2.6$. This value of p yields a spectral slope, $\beta \approx -0.8$, in the regime $\nu_{\rm X} \lesssim \nu_c$, which is roughly consistent with both the optical and X-ray spectral indices. On the other hand, the shallow prebreak optical and X-ray decline point to either an unusual hydrodynamic evolution (e.g., energy injection) or viewing angle effects (e.g., a structured jet viewed off axis) rather than different origins[20] for the optical and X-ray emission.

We find that an FS model with $p_{\rm FS} \approx 2.6$, $\epsilon_{\rm e} \approx 0.5$, $\epsilon_{\rm B} \approx 1.5 \times 10^{-3}$, $A_* \approx 0.1$, $E_{\rm K,iso} \approx 7.2 \times 10^{52}$ erg, and $\theta_{\rm jet} \approx 8°$ with energy injection periods from ≈0.1 to 1 day ($E \propto t$) and 1.4–9 days ($E \propto t$) matches the X-ray and optical light curves well (Figure 4). This model has $F_{\nu,\rm m,FS} \approx 15.5$ mJy, $\nu_{\rm c,FS} \approx 2.7 \times 10^{17}$ Hz (between the Einstein Probe Follow-up X-ray Telescope and NuSTAR bands), $\nu_{\rm m,FS} \approx 1.2 \times 10^{12} < \nu_{\rm opt}$, and $\nu_{\rm sa,FS} \approx 2.8 \times 10^{7}$ Hz $< \nu_{\rm radio}$ at 9 days, consistent with the soft X-ray and optical being on the same synchrotron segment.

In this model, the prompt efficiency relative to the energy of the entire outflow is tiny, $\eta_\gamma \approx 0.5\%$. Events exhibiting energy injection signatures are known to yield lower prompt efficiencies (e.g., T. Laskar et al. 2015). If the energy injection is due to shells of low Lorentz factor ejecta catching up and depositing energy into the FS (M. J. Rees & P. Meszaros 1998; R. Sari & P. Mészáros 2000), then this low prompt efficiency can be understood in a framework where the prompt emission (and hence $E_{\gamma,\rm iso}$) is dominated by emission from the fast-moving ejecta while the value of $E_{\rm K,iso}$ inferred from the afterglow modeling is sensitive to the total kinetic energy, including that residing in slower moving ejecta. Using the framework of T. Laskar et al. (2015), we find that the FS energy prior to the start of injection is $E_{\rm K,iso} \approx \times 10^{51}$ erg, which corresponds to a very reasonable value of $\eta_\gamma \approx 26\%$, further supporting the energy injection scenario.

3.2. Afterglow Evolution: Radio

This FS model underpredicts the majority of the radio observations at ≳16 days (Figure 4). Similar excess radio emission has frequently been ascribed to the RS (S. R. Kulkarni et al. 1999; E. Berger et al. 2003; S. Kobayashi & B. Zhang 2003b; A. Soderberg & E. Ramirez-Ruiz 2003; T. Laskar et al. 2013; D. A. Perley et al. 2014; A. van der Horst et al. 2014; T. Laskar et al. 2016, 2019a, 2019b; J. S. Bright et al. 2023; R. Gill & J. Granot 2023). The observed evolution of the peak flux ($F_{\rm peak} \sim t^{-1.5}$) and peak frequency ($\nu_{\rm peak} \sim t^{-0.6}$) of the radio component is slower than expected from a standard RS model, an effect plaguing several previous RS studies (T. Laskar et al. 2013; D. A. Perley et al. 2014). Following the spectacular failure of standard RS models for GRB 221009A (J. S. Bright et al. 2023; T. Laskar et al. 2023; L. Rhodes et al. 2024), an RS in a jet with angular structure was invoked to explain the radio emission in that event (R. Gill & J. Granot 2023; B. Zhang et al. 2024). We implement the analytical model of B. Zhang et al. (2024) (C. Rohde et al. 2026, in preparation[21]) and present a structured-jet RS model with a

[18] For arbitrary k, $\alpha = -[3(p-1)/4 + k/(8–2k)]$ for $\nu_{\rm m} < \nu_{\rm obs} < \nu_{\rm c}$ and $\alpha = (2–3p)/4$ for $\nu_{\rm obs} > \nu_{\rm c}$. In the latter case ($\nu_c < \nu_{\rm opt}$), the observed optical spectral index of $\beta \approx -1$ implies $p \approx 2$ and predicts $\alpha \approx -1$, inconsistent with the observed shallow optical decline. In the former case ($\nu_X < \nu_c$), the spectral index implies $p \approx 3$ and requires $k \approx 10$, where the underlying R. D. Blandford & C. F. McKee (1976) solution breaks down.

[19] We note that Einstein Probe Follow-up X-ray Telescope finds a harder spectral index at ≈2.5 days, indicating either an evolution in $\beta_{\rm X}$ with time or a systematic effect. Since the NuSTAR observation spans a wider frequency range (3–79 keV), we proceed with the latter in our analysis.

[20] The X-ray light curve exhibits a late-time rebrightening (beginning within 10–27 days; R. Jayaraman et al. 2026b; G. Waratkar et al. 2026), which may be evidence for shock interaction or a separate emission component.

[21] On GitHub: https://github.com/rohdog2003/rsjetstruct; the version for the current study is archived on Zenodo (C. Rohde et al. 2026).

deceleration time of $t_{\rm dec} \approx 4.3$ days, which roughly matches the radio SEDs, in Figure 4.

This model has $F_{\nu{\rm m,RS}} \approx 133$ mJy, $\nu_{\rm sa,RS} \approx 30$ GHz, $\nu_{\rm m,RS} \approx 8$ GHz, $\nu_{\rm c,RS} \approx 1.4 \times 10^{14}$ Hz, and $p_{\rm RS} \approx 2.5$, with a jet-break time of $t_{\rm jet} \approx 19$ days (consistent with the FS). The dynamical evolution is characterized by $g \approx 1.2$ and $k_\epsilon \approx 2$, where the bulk Lorentz factor of the shocked ejecta evolves with shock radius R as $\Gamma_{\rm ej} \propto R^{-g}$ following deceleration, while $E_{\rm k,iso}(\theta) \propto \theta^{-k_\epsilon}$ parametrizes the angular distribution of the ejecta isotropic-equivalent kinetic energy.

For completeness, we consider an alternate scenario where the radio flux is dominated by FS-like emission in Appendix C. We find that any viable FS model that matches the radio emission will underpredict the X-ray and optical light curves, requiring a separate emission component and equal or greater complexity than the FS+RS model discussed above. These models may be distinguishable via future polarimetry observations that measure the time dependence of Π_L.

4. Discussion

Our polarization observations offer two independent novel probes of the magnetic structure of the jet and its environment: Π_0 and RM. We now discuss possible interpretations of these measurements.

4.1. Polarimetric Constraints on the Magnetic Field Coherence Scale

Our afterglow model indicates that the radio emission is entirely dominated by the RS component at the time of our radio polarimetric measurement (19.2 days). In the presence of global ordered fields, the maximum fractional polarization fraction of synchrotron radiation in the optically thin regime ($\nu_{\rm obs} > \nu_{\rm sa}$), $\Pi_{\rm thin} = (p + 1)/(p + 7/3) \approx 0.72$ for $p \sim 2.5$ (A. G. Pacholczyk 1970; G. B. Rybicki & A. P. Lightman 1986; see also Appendix B). As we discussed above, the decrease in Π_L close to and below the peak is consistent with SSA depolarization (Section 2.2 and Appendix B) and an intrinsic polarization $\Pi_0 = (3.2 \pm 0.2)\%$, implying that the net polarization we observe on the optically thin segment is much less than the theoretical maximum of $\Pi_{\rm thin}$.

Following T. Laskar et al. (2019a), we consider a model in which the observed polarization arises from the combined emission of intrinsically polarized, mutually incoherent regions, each characterized by a magnetic field that is ordered over a typical angular scale, $\theta_{\rm B}$ (J. Granot & A. Königl 2003; E. Nakar & Y. Oren 2004; J. Granot & G. B. Taylor 2005). The number of patches contributing to the observed emission at time t is $N \sim (\Gamma_{\rm ej}(t)\theta_{\rm B})^{-2}$, where $\Gamma_{\rm ej}(t) \approx \Gamma_{\rm sh}(t)(t/t_{\rm dec})^{-[g-(3-k)/2]/[(4-k)(2g+1)]} \propto t^{-0.1}$ (for $g = 1.2$ and $k = 2$) is the ejecta Lorentz factor (S. Kobayashi 2000; J. Granot & G. B. Taylor 2005). In our FS+RS model, $\Gamma_{\rm sh} \approx 5.4$ at 19.2 days, implying $\Gamma_{\rm ej} \approx 4.7$ at that time.

The observed polarization from N patches is a random walk of N steps in the QU plane, such that $\Pi_{\rm L,obs}/\Pi_{\rm thin} \sim 1/\sqrt{N}$. Assuming a maximum intrinsic polarization of 72% for $p \sim 2.5$, this corresponds to $N \approx 500$ and implies $\theta_{\rm B} \sim 10^{-2}$. This measurement has a statistical uncertainty of ≈10%, but larger systematic uncertainties from the RS dynamics and the stochasticity of the 2D random walk. This value of $\theta_{\rm B}$ is an order of magnitude larger than $\theta_{\rm B} \approx 10^{-3}$ inferred from the ALMA polarimetry measurement of GRB 190114C (T. Laskar et al. 2019a); however, in that case, the observation took place at $\approx 7 \times 10^{-2}$ days in the rest frame and at $t \ll t_{\rm jet}$, whereas our VLA polarimetric observations of GRB 260310A are much later at 16.6 days in the rest frame and at a time comparable with the jet break, when considerable sideways spreading may take place (J. E. Rhoads 1999).

In Section 2.2, we interpreted the decrease of $\Pi_L(\nu)$ with decreasing frequency as arising from SSA (Figure 3). Combined with the above patchy shell model, this predicts that the polarization should rise again below $\nu_{\rm sa}$ to a fraction $(p + 7)(p + 1)^{-1}(6p + 13)^{-1} \approx 0.13$ (for $p = 3.1$; see Appendix B) of its value (Π_0) on the optically thin segment. For $\Pi_0 = 3.2\%$, this corresponds to ≈0.4%, just beyond the reach of our existing observations. Furthermore, the polarization position angle is expected to rotate by 90° across $\nu_{\rm sa}$. Lower-frequency polarimetric observations may test this framework further.

We note that optical polarimetric observations of GRB 260310A at 2.89 days posttrigger yielded a nondetection with an upper limit of $\Pi_L < 1.5\%$ (M. Pursiainen et al. 2026). While dust along the LOS can depolarize optical emission, the Galactic extinction toward GRB 260310A is very low, and the transient is significantly offset from the center of its host galaxy (Figure 1), suggesting a minimal dust column from either the MW or the host interstellar medium (ISM). We therefore do not expect dust-induced depolarization to significantly affect the optical polarization measurement for this event. Since SSA and Faraday depolarization are not relevant at optical wavelengths, we expect $\Pi_{\rm L,opt} \approx \Pi_{\rm L,radio}$ if the radio and optical emission are spatially colocated. In our FS+RS model, the optical emission is dominated by the FS at ∼3 days; since the FS is not expected to be strongly polarized (C. G. Mundell et al. 2013; R. Gill et al. 2021), this provides a natural explanation for the nondetection of optical polarization in this event. On the other hand, in any plausible models where the optical and radio emission arise from the same population of nonthermal electrons, the optical limit of $\Pi_{\rm L,opt} < 1.5\%$ at 2.89 days relative to $\Pi_{\rm L,radio} \approx 3\%$ at 19.2 days would imply genuine temporal evolution of the polarization and would require the magnetic field structure along the LOS to change over this period.

4.2. Constraints on Faraday Depolarization and the Origin of the High RM

The high RM, ${\rm RM}_{\rm int} \approx -8.3 \times 10^3$ rad m^{-2}, corresponds to a large rotation of χ. If the Faraday screen were colocated with the emitting region, we would expect strong Faraday depolarization across the source due to the differing paths of photons through the jet; however, the expected resulting deviations from $\chi \propto \lambda^2$ are not observed (Figure 3). Instead, the observed frequency dependence of $\Pi(\nu)$ is well explained by SSA depolarization, itself expected given clear SSA signatures in the radio SEDs (Figure 4). This suggests a Faraday screen external to the emitting region and allows us to quantify the coherence of such a screen. In the presence of stochastic RM variations of strength $\sigma_{\rm RM}$, we expect $\Pi_L \sim \Pi_0 e^{-2\sigma_{\rm RM}^2\lambda^4}$ (B. J. Burn 1966). The absence of strong Faraday depolarization at 11 GHz implies $2\sigma_{\rm RM}^2\lambda^4 \ll 1$ at that frequency, requiring $\sigma_{\rm RM} \lesssim 10^3$ rad m^{-2}. Relative to the observed RM, this implies a Faraday screen that is coherent at ≈15%. We caution that this estimate is weakened if some of the observed drop in Π_L at ≲11 GHz is instead due to Faraday depolarization (we discuss this scenario further in Appendix C). Further observations with a broader wavelength coverage may help disentangle these possibilities.

In the following, we proceed under the assumption that the Faraday screen is external to the emitting region, and we explore the physical origin of the large observed RM by assessing several plausible scenarios for the magnetized medium responsible for the Faraday rotation. Following the parameterization described in J. Granot & G. B. Taylor (2005), we can relate the RM to physical quantities through the expression

$$\mathrm{RM} = \frac{812}{(1+z)^2} \int_0^L \left(\frac{n_e}{\mathrm{cm}^{-3}}\right)\left(\frac{B_\parallel}{\mathrm{mG}}\right)\left(\frac{dl}{\mathrm{pc}}\right) \mathrm{rad\ m^{-2}}, \quad (2)$$

where L is the distance from the source to the end of the magnetized medium, n_e is the free electron number density, $B_\parallel$ is the magnetic field strength along the LOS, and dl is the incremental LOS path length from the source to the observer.

First, we consider the case where the radio emission is produced in the RS and the RM is produced by the shocked CSM behind the FS. At the time of our polarimetric measurements (19.2 days), our FS+RS model yields $\Gamma_{\rm FS} \approx 5.4$, a shock radius of $R_{\rm sh} \approx 10^{19}$ cm, and a postshock magnetic field of $B \approx 1.4$ mG. The density of the CSM at $R_{\rm sh}$ is $n_{\rm ext} \approx 3 \times 10^{-4}\ \mathrm{cm}^{-3}$, implying a postshock density, $n' \approx 4\Gamma_{\rm FS} n_{\rm ext} \approx 5.8 \times 10^{-3}\ \mathrm{cm}^{-3}$. Approximating the shocked ISM as a shell of proper thickness, $R \sim R_{\rm sh}/\Gamma_{\rm sh} \sim 2 \times 10^{18}$ cm, we estimate $\mathrm{RM_{FS}} \approx 3\ \mathrm{rad\ m^{-2}}$. This is much smaller than the observed value of $|\mathrm{RM}| \approx 6.3 \times 10^3\ \mathrm{rad\ m^{-2}}$, implying that the shocked CSM behind the FS cannot be responsible for the observed Faraday rotation.

The ISM of the host galaxy could, in principle, contribute significantly to the observed RM. In the MW, sight lines at low Galactic latitudes through the dense, magnetized ISM of the disk can produce RMs in excess of $\sim$100–1000 rad m^{-2} (N. Oppermann et al. 2012). Pulsar studies have shown Galactic LOS magnetic field strengths to be of the order of a few μG (e.g., R. J. Rand & S. R. Kulkarni 1989; H. Ohno & S. Shibata 1993; J. L. Han et al. 2004; L. Harvey-Smith et al. 2011). From Figure 1, we can see that GRB 260310A is well offset from the center of its host galaxy, placing it in a region where the ISM column density is expected to be substantially lower than along sight lines through the inner disk. We therefore suspect that the host galaxy ISM is an unlikely origin for the bulk of the observed RM, assuming the host galaxy shares a similar Faraday rotation map to that of the MW.

An alternative explanation for the large RM is the presence of a dense, magnetized region local to the GRB progenitor. One such environment is an H II region, where the massive stellar progenitors to Ic-BL supernovae associated with LGRBs are thought to originate (H. Zinnecker & H. W. Yorke 2007). The intense UV radiation and stellar winds from the massive progenitor can ionize and dynamically shape the surrounding medium, driving turbulent interactions within the ambient gas and dust (H. Zinnecker & H. W. Yorke 2007). This process enhances the free electron density and magnetic field strength, naturally giving rise to elevated Faraday RMs (exceeding several hundred rad m^{-2} in Galactic H II regions; L. Harvey-Smith et al. 2011).

Modeling of the X-ray afterglows of long-duration GRBs has shown that their progenitors reside within dense regions of photoionized gas that span sizes of 5–100 pc and free electron densities of $n_e \sim 10^2$–$10^4\ \mathrm{cm}^{-3}$ (A. L. Thakur et al. 2026). Independently, studies of magnetic field strengths in Galactic H II regions indicate that B fields in these environments can range from $\sim$1 to 100 μG (e.g., C. Heiles et al. 1981; L. Harvey-Smith et al. 2011; R. Devaraj et al. 2021). For these parameters, the expected RM spans from $\sim 4 \times 10^2$ to $\sim 8 \times 10^7\ \mathrm{rad\ m^{-2}}$, comfortably encompassing the observed value of $|\mathrm{RM_{int}}| \approx 8.3 \times 10^3\ \mathrm{rad\ m^{-2}}$. Our observed RM is therefore fully consistent with the population of H II regions previously associated with long GRBs and supports a massive star progenitor for GRB 260310A. If the RM is predominately produced in an H II region surrounding the GRB, we would expect it to remain constant in time. Future multifrequency polarimetry observations can thus test this scenario and distinguish it from alternate GRB jet models that might allow some RM contribution from within the jet itself.

5. Conclusions

We report the detection of linear polarization in GRB 260310A, marking the first centimeter polarization detection of a GRB and the first measurement of Faraday rotation in a GRB. We detect linearly polarized emission of 11–25 GHz, with the polarization fraction rising monotonically from $\Pi_L = (0.69 \pm 0.22)\%$ at 11 GHz to $\Pi_L = (3.18 \pm 0.18)\%$ at 25 GHz. The depolarization toward lower frequencies is likely dominated by SSA, which reduces the polarized intensity as the emitting region becomes optically thick.

Our observations reveal a frequency-dependent variation in the polarization angle consistent with Faraday rotation with $\mathrm{RM} = -6250 \pm 70\ \mathrm{rad\ m^{-2}}$ ($\mathrm{RM_{int}} = -8300 \pm 90\ \mathrm{rad\ m^{-2}}$ at the GRB redshift). The magnitude of this RM is consistent with linearly polarized emission propagating through a dense H II region, consistent with a massive star progenitor for GRB 260310A and pointing to a highly magnetized intervening medium.

These results demonstrate that GRB afterglows are linearly polarized across a broad range of radio frequencies, and that their polarization properties encode information about both the intrinsic jet magnetization and the intervening magnetized medium. Future multifrequency polarimetric monitoring campaigns spanning days to weeks will trace the coevolution of magnetic field geometry and afterglow emission, offering new constraints on the structure and dissipation of magnetic fields in GRB afterglows.

Acknowledgments

The National Radio Astronomy Observatory (NRAO) is a facility of the National Science Foundation operated under cooperative agreement by Associated Universities, Inc. Some observations reported here were obtained at the MMT Observatory, a joint facility of the University of Arizona and the Smithsonian Institution. K.D.A. gratefully acknowledges support from the Alfred P. Sloan Foundation. N.F. acknowledges support from the National Science Foundation Graduate Research Fellowship Program under grant No. DGE-2137419.

Software: `astropy` (Astropy Collaboration et al. 2013, 2018; Astropy Collaboration et al. 2022), `Jupyter` (F. Perez & B. E. Granger 2007), `matplotlib` (J. D. Hunter 2007), `numpy` (C. R. Harris et al. 2020), `pandas` (W. McKinney 2010), `python` (G. Van Rossum & F. L. Drake 2009), `scipy` (P. Virtanen et al. 2020), and `emcee` (D. Foreman-Mackey et al.

2013). Software citation information is aggregated using `The Software Citation Station` (https://www.tomwagg.com/software-citation-station/) (T. Wagg & F. S. Broekgaarden 2024; T. Wagg et al. 2025).

Appendix A
Polarization Calibration Verification and Systematic Checks

To assess the robustness of our polarization calibration, we performed a series of diagnostic checks on each calibrator. We describe these checks below and present the resulting calibrator SEDs and images in Figures 5, 6, and 7.

During calibration, the absolute polarization angle and fraction were set using 3C286, with Stokes I flux densities, polarization fractions, and polarization angles fixed to the frequency-dependent values tabulated by NRAO. To verify that this standard was faithfully transferred to the data, we imaged 3C286 across all observed frequencies and confirmed that the recovered polarization fractions and angles are consistent with the tabulated values to within the measurement uncertainties (Figure 5).

We next imaged the leakage calibrator J1407+2827, a source selected for its negligibly low intrinsic polarization, to verify the quality of the instrumental polarization (D-term) calibration. As expected, we detect a strong point source in Stokes I with no discernible emission in the Stokes Q or U images, which are instead consistent with noise (Figure 6). The 3σ upper limits on polarized emission from J1407+2827 correspond to $\lesssim 0.1\%$ of Stokes I, confirming that the instrumental leakage terms are properly calibrated to at least this level. For GRB 260310A, this leakage floor corresponds to $\sim 10\ \mu$Jy, which is comparable to the rms noise in the Stokes Q and U target images and well below our detected polarization signal of $\sim$60–270 μJy (Table 1).

As an additional verification that the detected polarization is astrophysical and not an artifact of the calibration or imaging procedure, we confirmed that the linear polarization signal in the target field is present both before and after self-calibration. As described in Section 2.2, self-calibration was performed on Stokes I (phase only), with the derived phase corrections subsequently applied to all Stokes parameters. The Stokes Q and U flux densities measured in each band are consistent before and after the application of the self-calibration solutions, with changes well within the measurement uncertainties.

We also imaged the phase calibrator J1357+7643, which was not used to calibrate the cross-hand (RL/LR) visibilities and therefore serves as an independent check on the polarization calibration. J1357+7643 exhibits weakly polarized emission at each observed frequency with a stable polarization angle across the band, consistent with a low RM. The absence of significant

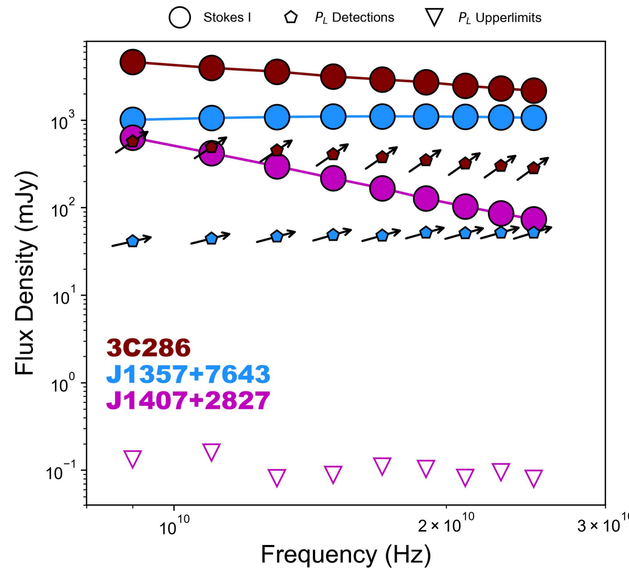

Figure 5. The SED for the bandpass, flux, and polarization angle calibrator 3C286, the gain calibrator J1357+7643, and the leakage calibrator J1407+2827 for the total intensity (Stokes I, circles) and linearly polarized intensity (Stokes P_L, pentagons). For the leakage calibrator, we show the 3σ upper limits on Stokes P_L (triangles). For the polarization flux densities, we also overlay the direction of the polarization angle (with the angle measured from the horizontal axis).

Faraday rotation in this calibrator LOS is consistent with the modest MW RM contribution expected at intermediate Galactic latitudes, further supporting our conclusion that the large RM observed toward GRB 260310A is intrinsic to the source or its local environment (Figure 7).

In Stokes V, we find that the images show low-level beam squint artifacts due to the offset in the RR and LL beam centers (common in off-axis feeds, which is the case for the VLA). This differential pointing introduces a systematic artifact in Stokes $V = (\mathrm{RR} - \mathrm{LL})/2$ that manifests as equal and opposite lobes at the position of the source in the Stokes V image. In our data, this artifact appears at the level of $\sim 0.2\%$ of Stokes I in only the bright calibrator sources. For the ~ 10 mJy flux density observed in GRB 2610310A, the same fractional level ($\sim 20\ \mu$Jy) falls below our linear polarization detections, and no beam squint artifact is detected in the target Stokes V images. Beam squint introduces a differential gain error between the parallel-hand correlations (RR and LL) and therefore contaminates only Stokes V, leaving the cross-hand products that form Stokes Q and U unaffected (J. M. Uson & W. D. Cotton 2008). The linear polarization detection and RM reported in this work are therefore not compromised by this low-level beam squint.

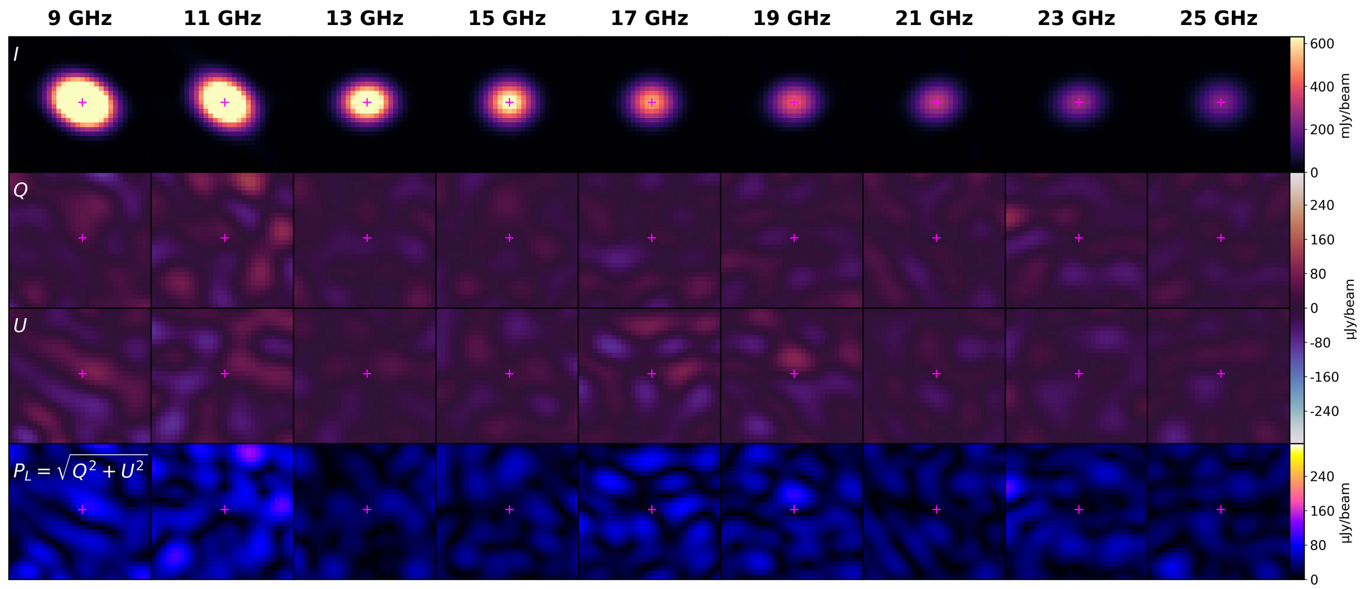

Figure 6. The same as Figure 2 but for the leakage calibrator J1407+2827.

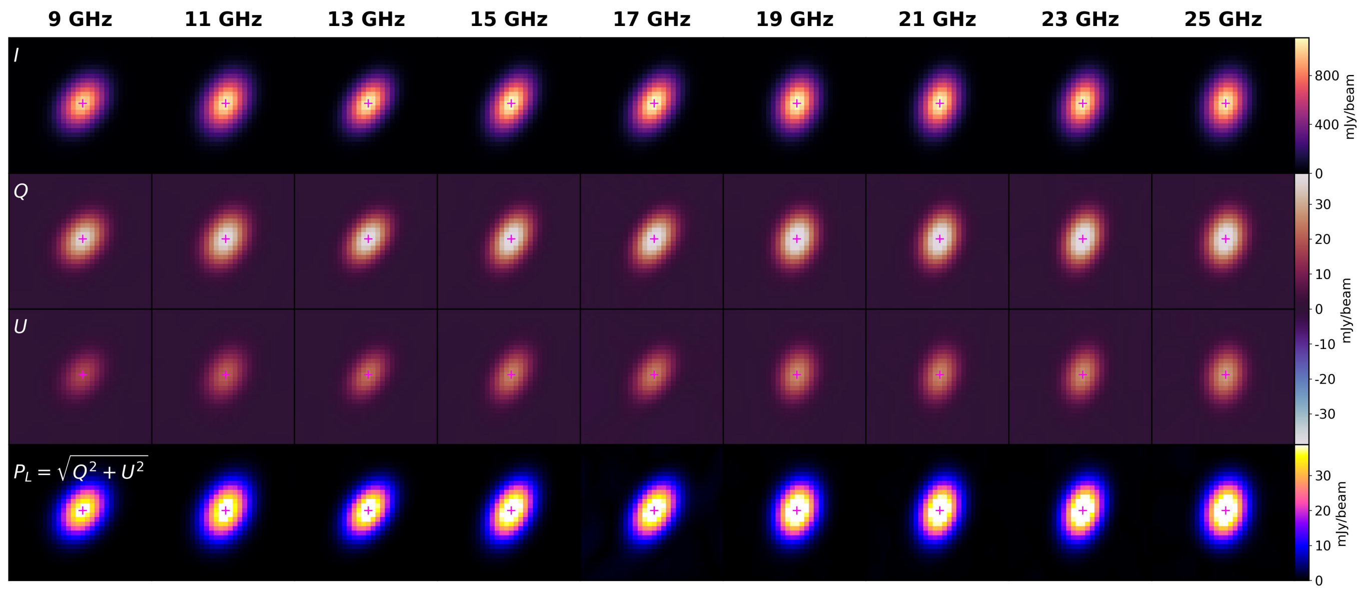

Figure 7. The same as Figure 2 but for the phase calibrator J1357+7643.

Appendix B
Frequency-dependent Synchrotron Polarization with Self-absorption

Following A. G. Pacholczyk (1970), we derive a simple model for the frequency-dependent linear polarization fraction, $\Pi(\nu)$, of synchrotron emission in the presence of SSA. We start with the assumption of locally ordered magnetic fields and later relax this assumption to account for magnetic field anisotropies in the visible region. The model captures the transition between the optically thin and optically thick regimes and provides a convenient framework for forward modeling of Stokes parameters.

For a power-law electron distribution $N(\gamma) \propto \gamma^{-p}$, the emission ($j_\nu$) and absorption ($\alpha_\nu$) coefficients of the two orthogonally polarized modes perpendicular ($\perp$) and parallel ($\parallel$) to the magnetic field projected on the sky are proportional to

$$j_{\perp,\parallel} \propto 1 \pm \frac{p+1}{p+7/3}, \tag{B1}$$

$$\alpha_{\perp,\parallel} \propto 1 \pm \frac{p+2}{p+10/3}, \tag{B2}$$

where the $+$ sign corresponds to the $\perp$ mode and the $-$ sign to the $\parallel$ mode. We assume that the SSA is dominated by the same nonthermal electrons responsible for the synchrotron emission. In the basis aligned with the polarization eigenmodes, the fractional linear polarization is

$$\Pi = \frac{Q}{I} = \frac{I_\perp - I_\parallel}{I_\perp + I_\parallel} = \frac{S_\perp(1-e^{-\tau_\perp}) - S_\parallel(1-e^{-\tau_\parallel})}{S_\perp(1-e^{-\tau_\perp}) + S_\parallel(1-e^{-\tau_\parallel})}, \tag{B3}$$

where $S_{\perp,\parallel} \equiv j_{\perp,\parallel}/\alpha_{\perp,\parallel}$ is the source function, and $\tau_{\perp,\parallel} \equiv \alpha_{\perp,\parallel} L$ is the optical depth (for a common path length L) for each mode, respectively.[23]

In the optically thin limit, $I_\nu \to S_\nu \tau_\nu = j_\nu L$, and the fractional polarization

$$\Pi_{\rm thin} = \frac{j_\perp - j_\parallel}{j_\perp + j_\parallel} = \frac{j_R - 1}{j_R + 1} = \frac{p+1}{p+\frac{7}{3}}, \tag{B4}$$

where

$$j_R \equiv \frac{j_\perp}{j_\parallel} = \frac{1+\Pi_{\rm thin}}{1-\Pi_{\rm thin}} = \frac{3p+5}{2}. \tag{B5}$$

In the optically thick limit, $I_\nu \to S_\nu$, and the fractional polarization

$$\Pi_{\rm thick} = \frac{S_\perp - S_\parallel}{S_\perp + S_\parallel} = \frac{j_\perp/\alpha_\perp - j_\parallel/\alpha_\parallel}{j_\perp/\alpha_\perp + j_\parallel/\alpha_\parallel} = \frac{j_\perp\alpha_\parallel - j_\parallel\alpha_\perp}{j_\perp\alpha_\parallel + j_\parallel\alpha_\perp} = \frac{j_R - \alpha_R}{j_R + \alpha_R} = -\frac{3}{6p+13}, \tag{B6}$$

where the negative sign indicates a 90° rotation of the polarization angle relative to the optically thin case, and

$$\alpha_R \equiv \frac{\alpha_\perp}{\alpha_\parallel} = \frac{1-\Pi_{\rm thick}}{1+\Pi_{\rm thick}} j_R = \frac{3p+8}{2}. \tag{B7}$$

The total optical depth

$$\tau_\nu = \left(\frac{\nu}{\nu_{\rm sa}}\right)^{-(p+4)/2} = \frac{\tau_\perp + \tau_\parallel}{2}, \tag{B8}$$

where

$$\tau_\perp = \frac{2\tau_\nu \alpha_\perp}{\alpha_\perp + \alpha_\parallel} = \frac{2\tau_\nu \alpha_R}{1+\alpha_R}, \tag{B9}$$

$$\tau_\parallel = \frac{2\tau_\nu \alpha_\parallel}{\alpha_\perp + \alpha_\parallel} = \frac{2\tau_\nu}{1+\alpha_R}, \tag{B10}$$

and $\nu_{\rm sa}$ is the SSA frequency, which we define here by $\tau_\nu(\nu_{\rm sa}) = 1$. Equation (B3) for the fractional polarization as a function of frequency in the presence of SSA can then be written as

$$\Pi(\nu) = \frac{\Pi_0}{\Pi_{\rm thin}} \frac{S_R(1-e^{-\tau_\perp}) - (1-e^{-\tau_\parallel})}{S_R(1-e^{-\tau_\perp}) + (1-e^{-\tau_\parallel})}, \tag{B11}$$

where $S_R \equiv j_R/\alpha_R$, and $\Pi_0 < 1$ is a free parameter that accounts for the fact that the observed polarization may be lower than the theoretically predicted maximum value due to, e.g., stochastic variations in B in the source region contributing to observable emission (see Section 4.1). Since $\tau_\perp/\tau_\parallel = \alpha_R = (3p+8)/2 > 1$, the perpendicular mode becomes optically thick first (at a higher frequency), where the parallel mode is still optically thin. This differential optical depth effect leads to a null in $\Pi(\nu)$, where $I_\perp$ and $I_\parallel$ cancel at a frequency given by the solution of the expression

$$S_R(1 - e^{-\frac{2\alpha_R \tau_\nu}{1+\alpha_R}}) = 1 - e^{-\frac{2\tau_\nu}{1+\alpha_R}}. \tag{B12}$$

For a given value of p, we can calculate $\Pi_{\rm thick}$, $\Pi_{\rm thin}$, j_R, and α_R from Equations (B6), (B4), (B5), and (B7), respectively. Equations (B8), (B9), and (B10) together can be used to compute $\tau_\perp(\nu)$ and $\tau_\parallel(\nu)$. The total intensity in this framework (assuming the spectral peak is at $\nu_{\rm sa}$) is

$$I(\nu) = S_\nu(1-e^{-\tau_\nu}) = I_0\left(\frac{\nu}{\nu_{\rm sa}}\right)^{5/2}(1-e^{-\tau_\nu}), \tag{B13}$$

with τ_ν given by Equation (B8). Given the total intensity $I(\nu)$ and polarization fraction $\Pi(\nu)$, the Stokes parameters are

$$Q(\nu) = I(\nu)\,\Pi(\nu)\cos[2\chi(\nu)], \tag{B14}$$

$$U(\nu) = I(\nu)\,\Pi(\nu)\sin[2\chi(\nu)], \tag{B15}$$

where the polarization angle is given by

$$\chi(\nu) = \chi_0 + {\rm RM}\,\lambda^2, \tag{B16}$$

where $\lambda = c/\nu$, and RM is the rotation measure. The 90° rotation across $\nu_{\rm sa}$ is captured by the sign change in $\Pi(\nu)$ and therefore does not need to be explicitly included in $\chi(\nu)$.

Appendix C
Faraday Rotation from an SSA-peaked Relativistic Shock

As an alternative to the FS+RS model, we consider a scenario where the radio observations are dominated by FS-like emission. We find that an FS in a wind-like environment with $p \approx 2.4$, $\epsilon_{\rm e} \approx 0.1$, $\epsilon_{\rm B} \approx 0.1$, $A_* \approx 0.3$, $E_{\rm K,iso} \approx 1.1 \times 10^{51}$ erg, and $\theta_{\rm jet} \gtrsim 40°$ roughly matches the radio SEDs at ≈16–25 days. This FS-only model has $F_{\nu,{\rm m,FS}} \approx 31$ mJy and $\nu_{\rm sa,FS} \approx 4.7 \times 10^7$ Hz $< \nu_{\rm radio} < \nu_{\rm m,FS} \approx 9.4 \times 10^{12} < \nu_{\rm c,FS} \approx 5.5 \times 10^{13}$ Hz $< \nu_{\rm opt}$ at the time of our polarimetric observations (19.2 days). This model underpredicts the high-frequency (230 GHz) radio data as well as the optical and X-ray emission, requiring a separate component at those frequencies.

If the observed Faraday rotation were produced within the source, we can obtain an independent estimate of the magnetic field coherence scale by modeling the FS as a spherical shock traveling at Lorentz factor Γ into an ambient medium with density $\rho_{\rm ext}(R)$ as a function of the shock radius, R. The image of the source has an extent $R_\perp$ transverse to the LOS, corresponding to an observed angular radius of

$$\theta = \frac{R_\perp}{d_A}, \tag{C1}$$

where d_A is the angular diameter distance. In the following, we associate the spectral flux density at the SSA frequency ($\nu_{\rm sa}$) with blackbody emission, subsuming factors of order unity into a correction term, $\xi(p)$, such that, for electrons with Lorentz factor γ_a corresponding to emission at $\nu_{\rm sa}$, the brightness temperature in the comoving frame is given by

$$3k_B T'_b \simeq \xi m_e c^2 \gamma_a. \tag{C2}$$

The Doppler-boosted and redshifted brightness temperature is

$$T_{b,{\rm obs}} = \frac{\delta}{1+z} T'_b, \tag{C3}$$

[23] This derivation assumes that the intrinsic Faraday rotation is small over a distance of one photon mean free path, i.e., $d\chi_F/ds \ll \alpha$, where $d\chi_F/ds$ is the Faraday rotation per unit path length, and α is the mean absorption coefficient. See A. G. Pacholczyk (1970) for a broader treatment, including Faraday depolarization.

where $\delta \sim \Gamma(1 + \beta)$ is the Doppler factor. Taking the image to be a uniformly illuminated disk, the observed flux density is the product of the angular area multiplied by the intensity:

$$F_a = \pi\theta^2 \frac{2\nu_{\rm sa}^2}{c^2} kT_{b,{\rm obs}}. \tag{C4}$$

Solving for the electron Lorentz factor yields

$$\gamma_a = \frac{3F_a d_A^2(1+z)}{2\pi\xi m_e \nu_{\rm sa}^2 R_\perp^2 \delta} = 19\,\xi^{-1}\left(\frac{F_a}{10.3\ {\rm mJy}}\right)\left(\frac{\nu_{\rm sa}}{13\ {\rm GHz}}\right)^{-2} \times\left(\frac{R_\perp}{1.5\times10^{17}\ {\rm cm}}\right)^{-2} \times\left(\frac{d_A}{1.7\times10^{27}\ {\rm cm}}\right)^2\left(\frac{\delta}{2.5}\right)^{-1}\left(\frac{1+z}{1.153}\right). \tag{C5}$$

Inverting the synchrotron characteristic frequency (assuming a pitch angle of 90°),

$$\nu(\gamma) = \frac{\delta}{1+z}\frac{3eB'}{4\pi m_e}\gamma^2, \tag{C6}$$

yields the following for the magnetic field,

$$B' = \frac{4\pi m_e}{3e}\frac{(1+z)\nu_{\rm sa}}{\delta\gamma_a^2} = 4.1{\rm G}\ \xi^2\left(\frac{F_a}{10.3\ {\rm mJy}}\right)^{-2}\left(\frac{R_\perp}{1.5\times10^{17}\ {\rm cm}}\right)^4 \times\left(\frac{d_A}{1.7\times10^{27}\ {\rm cm}}\right)^{-4}\left(\frac{\delta}{2.5}\right)\left(\frac{\nu_{\rm sa}}{13\ {\rm GHz}}\right)^5\left(\frac{1+z}{1.153}\right)^{-1}. \tag{C7}$$

For a strong relativistic shock, the proper postshock number density is

$$n'_{\rm ps} \simeq 4\Gamma n_{\rm ext}. \tag{C8}$$

The Faraday RM for a uniform shell of proper thickness ΔR is

$${\rm RM} = \frac{e^3}{8\pi^2\epsilon_0 m_e^2 c^3}\int\frac{n'_e B'_\parallel dl'}{(1+z)^2} \simeq \frac{e^3}{8\pi^2\epsilon_0 m_e^2 c^3} \times\frac{\eta_B n'_{\rm ps} B'\Delta R}{(1+z)^2} \simeq \frac{2.63\times10^3\eta_B}{(1+z)^2} \times\frac{n'_{\rm ps}}{{\rm cm}^{-3}}\frac{B'}{\rm G}\frac{\Delta R}{10^{16}\ {\rm cm}}\ {\rm rad\ m^{-2}}, \tag{C9}$$

where we have written $B'_\parallel = \eta_B B'$. Substituting the shock-jump density and the SSA-derived magnetic field, we have

$${\rm RM_{obs}} \simeq 7.6\times10^4\left(\frac{F_a}{10.3\ {\rm mJy}}\right)^{-2} \times\left(\frac{\nu_{\rm sa}}{13\ {\rm GHz}}\right)^5\left(\frac{1+z}{1.153}\right)^{-3} \times\eta_B\xi^2\left(\frac{R_\perp}{1.5\times10^{17}\ {\rm cm}}\right)^4\left(\frac{d_A}{1.7\times10^{27}\ {\rm cm}}\right)^{-4} \times\left(\frac{\delta}{2.5}\right)^2\left(\frac{n_{\rm ext}}{0.15\ {\rm cm}^{-3}}\right)\left(\frac{\Delta R}{10^{16}\ {\rm cm}}\right){\rm rad\ m^{-2}}, \tag{C10}$$

where we have scaled the values to the image size and external medium density predicted for the FS using the R. D. Blandford & C. F. McKee (1976) solution at 19.2 days following the formalism of J. Granot & R. Sari (2002). Relative to the measured RM $\sim 6.3 \times 10^3$ rad m^{-2}, this implies $\eta_B \sim 0.1$. Finding $\eta_B < 1$ implies that Faraday rotation in an FS-produced B field may generate the observed RM in this model. However, we note that this conclusion is strongly sensitive to the image size ($R_\perp$) and to the unknown thickness of the region responsible for the Faraday rotation, ΔR.

ORCID iDs

Collin T. Christy https://orcid.org/0000-0003-0528-202X
Tanmoy Laskar https://orcid.org/0000-0003-1792-2338
Kate D. Alexander https://orcid.org/0000-0002-8297-2473
Noah Franz https://orcid.org/0000-0003-4537-3575
Jonathan Granot https://orcid.org/0000-0001-8530-8941
Ryan Chornock https://orcid.org/0000-0002-7706-5668
Raffaella Margutti https://orcid.org/0000-0003-4768-7586
Ramandeep Gill https://orcid.org/0000-0003-0516-2968
Jeniveve Pearson https://orcid.org/0000-0002-0744-0047
Edo Berger https://orcid.org/0000-0002-9392-9681
Wen-fai Fong https://orcid.org/0000-0002-7374-935X
Coleman Rohde https://orcid.org/0009-0007-3919-8439
Patricia Schady https://orcid.org/0000-0002-1214-770X

References

Amati, L. 2006, MNRAS, 372, 233
Arimoto, M., Asano, K., Kawabata, K. S., et al. 2024, NatAs, 8, 134
Astropy Collaboration, Price-Whelan, A. M., Lim, P. L., et al. 2022, ApJ, 935, 167
Astropy Collaboration, Price-Whelan, A. M., Sipőcz, B. M., et al. 2018, AJ, 156, 123
Astropy Collaboration, Robitaille, T. P., Tollerud, E. J., et al. 2013, A&A, 558, A33
Atteia, J.-L., Moreno Méndez, E., Lincetto, M., et al. 2026, GCN, 43981, 1
Barth, A. J., Sari, R., Cohen, M. H., et al. 2003, ApJL, 584, L47
Becerra, R. L., Watson, A. M., Angulo Valdez, C., et al. 2026, GCN, 43991, 1
Berger, E., Soderberg, A. M., Frail, D. A., & Kulkarni, S. R. 2003, ApJL, 587, L5
Bersier, D., McLeod, B., Garnavich, P. M., et al. 2003, ApJL, 583, L63
Birenbaum, G., Granot, J., & Beniamini, P. 2026, A&A, 706, A145
Björnsson, G., Hjorth, J., Pedersen, K., & Fynbo, J. U. 2002, ApJL, 579, L59
Blandford, R. D., & McKee, C. F. 1976, PhFl, 19, 1130
Bright, J. S., Rhodes, L., Farah, W., et al. 2023, NatAs, 7, 986
Brivio, R., Malesani, D., Izzo, L., et al. 2026, GCN, 44004, 1
Brosio, A., Tripodi, M. A., Savaglio, S., et al. 2026a, GCN, 44021, 1
Brosio, A., Tripodi, M. A., Savaglio, S., et al. 2026b, GCN, 44067, 1
Burn, B. J. 1966, MNRAS, 133, 67

CASA Team, Bean, B., Bhatnagar, S., et al. 2022, PASP, 134, 114501
Covino, S., & Gotz, D. 2016, A&AT, 29, 205
Covino, S., Lazzati, D., Ghisellini, G., et al. 1999, A&A, 348, L1
de Ugarte Postigo, A., Geier, S., Izzo, L., et al. 2026b, GCN, 44124, 1
de Ugarte Postigo, A., Izzo, L., Martin-Carrillo, A., et al. 2026a, GCN, 43984, 1
Devaraj, R., Clemens, D. P., Dewangan, L. K., et al. 2021, ApJ, 911, 81
Fermi GBM team 2026, GCN, 43951, 1
Foreman-Mackey, D., Hogg, D. W., Lang, D., & Goodman, J. 2013, PASP, 125, 306
Frail, D. A., Kulkarni, S. R., Nicastro, L., Feroci, M., & Taylor, G. B. 1997, Natur, 389, 261
Freeberg, M., Serrau, M., Turpin, D., et al. 2026, GCN, 44248, 1
Gabuzda, D. C., Knuettel, S., & Reardon, B. 2015, MNRAS, 450, 2441
Giarratana, S., Giroletti, M., Ghirlanda, G., et al. 2026, GCN, 44045, 1
Gill, R., & Granot, J. 2023, MNRAS, 524, L78
Gill, R., Kole, M., & Granot, J. 2021, Galax, 9, 82
Granot, J. 2003, ApJL, 596, L17
Granot, J., & Königl, A. 2003, ApJL, 594, L83
Granot, J., & Sari, R. 2002, ApJ, 568, 820
Granot, J., & Taylor, G. B. 2005, ApJ, 625, 263
Gruzinov, A., & Waxman, E. 1999, ApJ, 511, 852
Guelfand, M., Moreno Méndez, E., Becerra, R. L., et al. 2026, GCN, 44125, 1
Hamburg, R., & Meegan, C. 2026, GCN, 43975, 1
Han, J. L., Ferriere, K., & Manchester, R. N. 2004, ApJ, 610, 820
Harris, C. R., Millman, K. J., van der Walt, S. J., et al. 2020, Natur, 585, 357
Harvey-Smith, L., Madsen, G. J., & Gaensler, B. M. 2011, ApJ, 736, 83
Heiles, C., Chu, Y.-H., & Troland, T. H. 1981, ApJL, 247, L77
Hinds, K., Hall, X. J., Perley, D. A., et al. 2026, TNSAN, 65, 1
Hinds, K.-R., Perley, D. A., Ho, A. Y. Q., et al. 2026, GCN, 43977, 1
Ho, A., Keating, G., Alexander, K., et al. 2026, GCN, 44134, 1
Ho, A. Y. Q., Bremer, M., & Schroeder, G. 2026, GCN, 44057, 1
Hovatta, T., Lister, M. L., Aller, M. F., et al. 2012, AJ, 144, 105
Hsu, B., Shrestha, M., Andrews, J., et al. 2026, GCN, 43986, 1
Hunter, J. D. 2007, CSE, 9, 90
Izzo, L. 2026, GCN, 44003, 1
Jayaraman, R., Hinds, K.-R., Waratkar, G., et al. 2026b, GCN, 44234, 1
Jayaraman, R., Ho, A. Y. Q., Hinds, K.-R., et al. 2026a, GCN, 43994, 1
Jayaraman, R., Waratkar, G., Hinds, K.-R., et al. 2026c, GCN, 44095, 1
Kammoun, E., Waratkar, G., Jayaraman, R., Hinds, K.-R., & Ho, A. Y. Q. 2026, GCN, 44063, 1
Kobayashi, S. 2000, ApJ, 545, 807
Kobayashi, S., & Zhang, B. 2003a, ApJ, 597, 455
Kobayashi, S., & Zhang, B. 2003b, ApJL, 582, L75
Konno, R., Garrappa, S., Zimmerman, E. A., et al. 2026, GCN, 43974, 1
Kravchenko, E. V., Kovalev, Y. Y., & Sokolovsky, K. V. 2017, MNRAS, 467, 83
Kronberg, P. P., & Simard-Normandin, M. 1976, Natur, 263, 653
Kulkarni, S. R., Frail, D. A., Sari, R., et al. 1999, ApJL, 522, L97
Kumar, P., & Zhang, B. 2015, PhR, 561, 1
Lai, C.-H., Aryan, A., Lee, Y.-H., et al. 2026, GCN, 44002, 1
Laskar, T., Alexander, K. D., Berger, E., et al. 2016, ApJ, 833, 88
Laskar, T., Alexander, K. D., Gill, R., et al. 2019a, ApJL, 878, L26
Laskar, T., Alexander, K. D., Margutti, R., et al. 2023, ApJL, 946, L23
Laskar, T., Berger, E., Margutti, R., et al. 2015, ApJ, 814, 1
Laskar, T., Berger, E., Zauderer, B. A., et al. 2013, ApJ, 776, 119
Laskar, T., van Eerten, H., Schady, P., et al. 2019b, ApJ, 884, 121
Lazzati, D., Covino, S., di Serego Alighieri, S., et al. 2003, A&A, 410, 823
Li, J.-J., Chen, C., Cao, D.-L., et al. 2026, GCN, 43993, 1
Maiorano, E., Masetti, N., Palazzi, E., et al. 2006, A&A, 455, 423
Martin-Carrillo, A., Aasen, E., Brown, L., et al. 2026a, GCN, 44000, 1
Martin-Carrillo, A., Garcia-Valino, J. R., Aasen, E., et al. 2026b, GCN, 43979, 1
McKinney, W. 2010, in Proc. of the 9th Python in Science Conf., ed. S. van der Walt & J. Millman, 56
Méndez, E. M., Lincetto, M., Dornic, D., et al. 2026, GCN, 43980, 1
Mészáros, P. 2006, RPPh, 69, 2259
Meszaros, P., & Rees, M. J. 1993, ApJ, 405, 278
Michilli, D., Seymour, A., Hessels, J. W. T., et al. 2018, Natur, 553, 182
Minaev, P., Pozanenko, A. & GRB follow-up Team 2026, GCN, 44053, 1
Moskvitin, A., Spiridonova, O., Pozanenko, A., et al. 2026, GCN, 44006, 1
Mtchedlidze, S., Domínguez-Fernández, P., Du, X., et al. 2024, ApJ, 977, 128
Mundell, C. G., Kopač, D., Arnold, D. M., et al. 2013, Natur, 504, 119
Nakar, E., & Oren, Y. 2004, ApJL, 602, L97
O'Connor, B., Toshikage, S., Tanaka, M., et al. 2026, GCN, 44137, 1
Ohno, H., & Shibata, S. 1993, MNRAS, 262, 953
O'Neill, D., Ramsay, G., Ackley, K., et al. 2026, TNSTR, 2026, 1
Oppermann, N., Junklewitz, H., Robbers, G., et al. 2012, A&A, 542, A93
Pacholczyk, A. G. 1970, Radio Astrophysics. Nonthermal Processes in Galactic and Extragalactic Sources (Freeman)
Pankov, N., Volnova, A., Klunko, E., et al. 2026, GCN, 44073, 1
Passaleva, N., Yang, Y.-H., Shahamt, N., Troja, E. & ERC BHianca Team 2026a, GCN, 44058, 1
Passaleva, N., Yang, Y.-H., Shahamt, N., Troja, E. & ERC BHianca Team 2026b, GCN, 44104, 1
Perez, F., & Granger, B. E. 2007, CSE, 9, 21
Perley, D. A., Cenko, S. B., Corsi, A., et al. 2014, ApJ, 781, 37
Perley, D. A., Schroeder, G., & Laskar, T. 2026a, GCN, 44160, 1
Perley, D. A., Wagh, Y., Jayaraman, R., et al. 2026b, GCN, 44096, 1
Pursiainen, M., Malesani, D. B., Leloudas, G., et al. 2026, GCN, 43990, 1
Rand, R. J., & Kulkarni, S. R. 1989, ApJ, 343, 760
Rastinejad, J. C., Gompertz, B. P., Levan, A. J., et al. 2022, Natur, 612, 223
Rees, M. J., & Meszaros, P. 1994, ApJL, 430, L93
Rees, M. J., & Meszaros, P. 1998, ApJL, 496, L1
Rhoads, J. E. 1999, ApJ, 525, 737
Rhodes, L., Hughes, A., Fender, R., et al. 2026, GCN, 44005, 1
Rhodes, L., van der Horst, A. J., Bright, J. S., et al. 2024, MNRAS, 533, 4435
Rohde, C., Laskar, T., & Oliver, D. 2026, rsjetstruct: spectrum calculator for power law structured jet reverse shocks, bb0b566, Zenodo, doi: 10.5281/zenodo.20800413
Rol, E., Wijers, R. A. M. J., Vreeswijk, P. M., et al. 2000, ApJ, 544, 707
Rossi, E. M., Lazzati, D., Salmonson, J. D., & Ghisellini, G. 2004, MNRAS, 354, 86
Rybicki, G. B., & Lightman, A. P. 1986, Radiative Processes in Astrophysics (Wiley-VCH), 400
Salmonson, J. D. 2003, ApJ, 592, 1002
Salunke, S. K. H. H., Tembhurnikar, M., et al. 2026, GCN, 43958, 1
Sari, R. 1997, ApJL, 489, L37
Sari, R., & Mészáros, P. 2000, ApJL, 535, L33
Sari, R., & Piran, T. 1995, ApJL, 455, L143
Sari, R., & Piran, T. 1999, ApJ, 520, 641
Schroeder, G., Perley, D. A., & Laskar, T. 2026, GCN, 44235, 1
Serrau, M., Freeberg, M., Turpin, D., et al. 2026, GCN, 44112, 1
Soderberg, A., & Ramirez-Ruiz, E. 2003, MNRAS, 345, 854
Steele, I. A., Kopač, D., Arnold, D. M., et al. 2017, ApJ, 843, 143
Stein, R., Mo, G., Karambelkar, V., et al. 2026, GCN, 43996, 1
Thakur, A. L., Piro, L., Luminari, A., et al. 2026, NatAs, 10, 714
Troja, E., Fryer, C. L., O'Connor, B., et al. 2022, Natur, 612, 228
Urata, Y., Toma, K., Covino, S., et al. 2023, NatAs, 7, 80
Uson, J. M., & Cotton, W. D. 2008, A&A, 486, 647
Vallee, J. P. 1975, Natur, 254, 23
van der Horst, A., Paragi, Z., de Bruyn, A. G., et al. 2014, MNRAS, 444, 3151
Van Rossum, G., & Drake, F. L. 2009, Python 3 Reference Manual (CreateSpace)
Vernstrom, T., Gaensler, B. M., Rudnick, L., & Andernach, H. 2019, ApJ, 878, 92
Virtanen, P., Gommers, R., Oliphant, T. E., et al. 2020, NatMe, 17, 261
Volnova, A., Pankov, N., Klunko, E., et al. 2026, GCN, 44060, 1
Wagg, T., Broekgaarden, F., Van-Lane, P., Wu, K., & Gültekin, K. 2025, TomWagg/software-citation-station: v1.4, Zenodo, doi: 10.5281/zenodo.17654855
Wagg, T., & Broekgaarden, F. S. 2024, arXiv:2406.04405
Waratkar, G., Kammoun, E., Jayaraman, R., Hinds, K.-R., & Ho, A. Y. Q. 2026, GCN, 44278, 1
Watson, A. M., Dornic, D., Becerra, R. L., et al. 2026, GCN, 44001, 1
Wiersema, K., Covino, S., Toma, K., et al. 2014, Natur, 509, 201
Woosley, S. E., & Bloom, J. S. 2006, ARA&A, 44, 507
Yang, Y., Troja, E., Yin, Y.-H. I., et al. 2026, GCN, 44375, 1
Yang, Y.-P., Xu, S., & Zhang, B. 2023, MNRAS, 520, 2039
Zhang, B., Wang, X.-Y., & Zheng, J.-H. 2024, JHEAp, 41, 42
Zinnecker, H., & Yorke, H. W. 2007, ARA&A, 45, 481